Wear 526–527 (2023) 204931

Contents lists available at ScienceDirect

Wear

journal homepage: www.elsevier.com/locate/wear

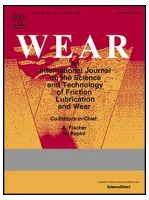

Wear performance under dry and lubricated conditions of duplex treatment TiN/TiCrN coatings deposited with different numbers of CrN interlayers on steel substrates

Seda Ataş Bakdemir [a,b,*], Doğuş Özkan [a], Cenk Türküz [c], Serdar Salman [d]

[a] National Defence University, Turkish Naval Academy, Tuzla, İstanbul, Turkey
[b] Marmara University, Metallurgy and Materials Engineering, Göztepe, İstanbul, Turkey
[c] Titanit Ultrahard Coatings Company, Güngören, İstanbul, Turkey
[d] National Defence University, Beşiktaş, İstanbul, Turkey

ARTICLE INFO

Keywords:
Duplex surface treatment
arc-PVD coatings
Multilayer coatings
TiN/TiCrN coatings
Wear mechanisms
ZDDP anti-Wear additive

ABSTRACT

Cold work steels are used in harsh conditions including high load, wear, corrosion, and mechanical stresses that can easily lead to degradation and wear of the material. Generally, multilayer ceramics coatings are attractive candidates to develop engineering components by combining positive characteristics of different coatings. In this study, the TiN/TiCrN coatings with the different number of CrN interlayers were successfully deposited on nitrided and non-nitrided DIN 1.2379 steel, and their wear behavior was investigated at dry and lubrication conditions under different loads. The relationship between coating architectures and coating characteristics was explored. The microstructure and composition of the specimens were studied using X-ray diffraction (XRD), scanning electron microscopy (SEM) with Energy dispersive X-ray analysis (EDX) and Atomic force microscopy (AFM).The nano-hardness were measured by nanoindenter, respectively. The adhesion and tribological behavior were evaluated using the Rockwell-C indentation and reciprocating tribometer tests, respectively. The results reveal that the nitrided samples with the TiN/TiCrN coatings with the different number of CrN interlayer showed much better wear resistance than the non-nitrided coatings at dry conditions. On the other hand, nitrided and nitride + coated TiN/TiCrN with the different number of CrN interlayer specimen showed better wear resistance at lubricated conditions. In addition, the fact that uncoated and nitrided steels have higher wear resistance at lubricated conditions than coated samples shows that TiN/TiCrN coatings are not proper even with a lubricant additive over a certain load value.

1. Introduction

The friction and wear losses have a great impact on the production efficiency of the tool steel manufacturing companies [1]. To overcome these losses ceramics coatings consisting of hard transition metal nitrides have been commercialized over the past decade [2]. Hard ceramic physical vapor deposited (PVD) coatings such as TiN have been intensively employed to enhance the surface and mechanical properties of the cutting tools and molds [3]. Moreover, heat generation and energy losses can be reduced by friction decrease using the hard PVD ceramic coatings in operating conditions [4]. Hard ceramic coatings can be deposited in single or multilayers with different metallic or ceramic interlayers to obtain lower friction and superior wear and corrosion resistance [5,6]. Furthermore, researchers have focused on nanostructured multi-layer ceramic coatings to prolong the effective life of tools over the past few years [7]. The researchers reported that adding a third element to TMN (M denotes for another metallic element) improved the microstructure and mechanical characteristics of ceramic hard coatings manufactured employing physical vapor deposition (PVD) techniques [8].

There have already been many publications available in the literature in which various elements such as Al, B, and Cr were doped to TiN to improve the coating's tribomechanical properties [9]. The stress which is essential to activate dislocations increase with the presence of a large number of grain boundaries and the agglomerated dislocation in a nanostructured coating. Each parameter that prevents of movement

* Corresponding author. National Defence University, Turkish Naval Academy, 34942, Tuzla, İstanbul, Turkey.
E-mail addresses: sabakdemir@dho.edu.tr (S. Ataş Bakdemir), dozkan@dho.edu.tr (D. Özkan), cenk.turkuz@titanit.com.tr (C. Türküz), ssalman@marmara.edu.tr (S. Salman).

https://doi.org/10.1016/j.wear.2023.204931
Received 10 August 2022; Received in revised form 1 April 2023; Accepted 18 April 2023
Available online 18 April 2023

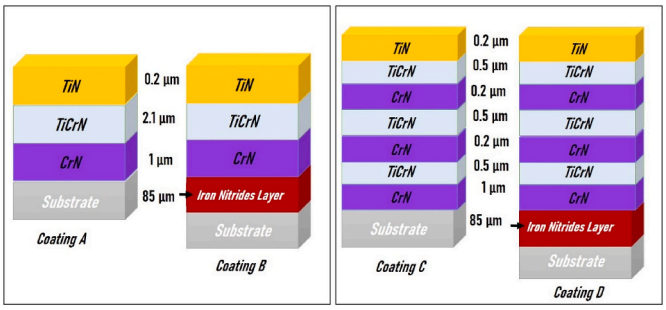

Fig. 1. Nomenclature and architecture of coatings.

dislocations supplies hardness increment [9,10]. TiCrN coating has enhanced mechanical properties such as high hardness, high-temperature oxidation resistance, and low friction coefficient due to consisting of a triple compound with 100% solid solubility of Ti and Cr [11,12]. This triple coating is very versatile because it can be deposited in a nanocrystalline structure more readily than binary materials [13]. The interstitial diffusion of chromium in the cubic face-centered TiN structure enhances the quality of the TiCrN coating [14]. The two common methods for producing (Ti, Cr) N coatings by cathodic arc evaporation are using a single alloy target composed of Cr and Ti and a multisource technique in which more than one single-phase target (i.e. Ti and Cr) [15,16].

Although there are many research works regarding the structural and mechanical properties of TiCrN films, few studies have reported the effect of TiCrN coatings produced by the cathodic arc-PVD method after the gas nitriding process [17,18]. Especially, deformations in the substrate can occur when the mechanical properties of the substrate, such as hardness and elastic modulus, are insufficient for the working circumstances, leading the coating to crack and flake before its lifetime [19]. Combining PVD coatings with a pre- or post-treatment can further enhance the coating properties. To improve the wear resistance of the substrates, a duplex treatment composed of gas nitriding can be used before the TiCrN coating [20,21].

The influence of coating structure and gas nitriding process on properties of TiN/TiCrN coatings were comprehensively investigated mechanically, chemically at different experimental environments. For this purpose, two different TiN/TiCrN coating structure were deposited on the nitrided and non-nitrided samples and the tribological properties of the coating were determined at different load parameters and dry/lubricated conditions in this study.

2. Experimental procedures

2.1. Materials and coating deposition

The substrate material used in this study was DIN 1.2379 cold work steel and the dimensions of the specimens were 35 mm in diameter and 5 mm in thickness. The specimens were heat treated at 525 °C for 2 h and quenched in air. The specimens were ground mechanically with SiC sandpaper ranging 120 to 1200 and polished to mirror-like surfaces with 1, 3, and 6 µm diamond polishing fluid to achieve the appropriate surface conditions. Then the specimens were cleaned in ultrasonic bath with ethanol and acetone for 20 min. A duplex process was performed on the samples in two steps; firstly, gas nitriding process was applied and this was followed by a PVD coating of different structure of TiN/TiCrN. The nitriding process was carried out by using the method of two-step controlled gas nitriding in an ammonia (NH_3) atmosphere. Specimens were heated to 1 h at 450 °C and 7 h at 530 °C, respectively and cooled gradually to room temperature under the same atmosphere. The TiN/TiCrN coatings were deposited on specimens by a commercial PVD cathodic arc process (Interatom PVD 32), utilizing titanium (99.97%) and chromium (99.95%) cathodes and high purity nitrogen gas. In addition to the specimens of base steel and nitrided steel, the Si (1 0 0) wafers were placed into the coating chamber to determine the coating growth morphologies. Nomenclature of the specimens, schematic illustration of the coating architectures and coating thickness per layer were showed in Fig. 1.

The designations 'coating A and B′ were used for TiN/TiCrN coatings deposited on the CrN adhesion layer, while 'coating C and D′ were used for TiN/TiCrN coatings with two additional CrN interlayers on the CrN adhesion layer.

The deposition chamber was heated to 350 °C and then evacuated to a base pressure of 4.5×10^{-5} mbar prior to the coating process in order to provide a contamination-free atmosphere. In an effort to further enhance the substrate-coating adhesion, Ar etching (Glow Discharge) and ion bombardment under high bias voltage (>700 V) were also performed within the deposition chamber. The distance from target to substrate holder was maintained at 150 mm. Nitrogen (N_2) and Argon (Ar) were used as reactive and process gases during deposition time, respectively. The details of coating parameters used in this study were given in Table 1.

The TiN/TiCrN coating without CrN interlayer was deposited with an average thickness of ~3.22 µm and the TiN/TiCrN coating with two CrN interlayers was deposited with an average thickness of ~3.17 µm. The purpose of depositing CrN as a first layer is that the presence of an interlayer, which reduces the effect of substrate defects and improves surface quality, provides high adhesion between the coating and the substrate [22]. The purpose of TiN layer on top of the coating with less than 0.5 µm thickness was to obtain both a harder top layer with more abrasion resistance and the color uniformity.

2.2. Nanoindentation and adhesion test

The hardness and elastic modulus of the coatings were measured on a CSM NHTX indenter device, by using Berkovich indenter. Considering the different layers of the coatings, indenter tests were carried out at different load values (15 mN–90 mN) and penetration depths. The hardness and elastic modulus were estimated following the Oliver and

Table 1
Parameters of coatings.

Sample	Target type and number	Deposition time for each layer (min)	Temperature (°C)	Nitrogen Gas Flow (sccm)	Bias Voltage (V)	Cathod Amper (A)	Working Pressure (mbar)
Coating A-B	4 Cr	45	380	285	−150	60	5×10^{-2}
	4 Cr, 4 Ti	50	395	320			
	4 Ti	20	365	205			
Coating C-D	4 Cr	45	350	280	−150	60	5×10^{-2}
	4 Cr, 4 Ti	15	390	315			
	4 Cr	5	390	280			
	4 Cr, 4 Ti	15	410	315			
	4 Cr	5	400	275			
	4 Cr, 4 Ti	15	420	315			
	4 Ti	15	415	205			

Pharr method for the analysis of the load-displacement curves. The indenter test was repeated five times for each specimen to obtain average hardness and elastic modulus. The adhesion strength of coatings was evaluated by Rockwell-C indentation test with a load of 150 kgf. This method was standardized by the Union of German Engineers (Verein Deutscher Ingenieure, VDI), a Rockwell C-type diamond cone indenter was used as indenter. The results were analyzed through an optical microscope and the adhesion level was ranked between HF1 and HF6 according to the level of cracks and the presence of coating detachments around the indention area [23,24].

2.3. XRD and SEM/EDX

An X-ray diffractometer (Bruker D8 Advance) was used to determine the crystalline phase of the coatings with Cu Kα radiation (1.542 Å). The diffraction patterns of all samples were recorded for values at 2θ between 10° and 80°, in the continuous recording mode. The position and intensity of the diffraction lines characteristic of each phase were determined with Xpert High Score Data. Additionally, the crystallite sizes of the coatings (d), which were calculated from the average of all peaks using Debye- Scherrer's formula ($d = K\lambda/\beta\cos\theta$), (d is the size of the crystallite, K is Scherrer constant 0.94, λ is the X-ray wavelength which in this case is 1.54 Å produced by a copper pole, β is the full width of half maximum (FWHM) of the XRD peaks, and θ represents the angles where the peaks are positioned [25].

Scanning electron microscopy (SEM) (JEOL FIB-4601 MultiBeam) was used to investigate the coating surfaces, wear scar morphologies and cross-sectional images of the coatings through an acceleration voltage of 15 kV. Additionally, chemical analysis was carried out on different areas using an energy dispersive X-ray spectrometer (EDX) (Oxford Xmax-N). The total film thickness was evaluated by the Calotest in addition to SEM analysis. For this purpose, the specimens were exposed to sliding friction, resulting in abrasive wear made by a hardened steel sphere with a diameter of 20 mm doped with the 0.25 μm diamond slurry for 60 s. Atomic force microscopy (AFM-Nanosurf Flex-5) and an optical microscope (Nikon LV-150) were used to analyze surface topography.

2.4. Wear test

The tribological tests were carried out under dry and lubricated conditions. The wear and friction tests were performed under different normal loads of 15, 20 (for dry sliding) 30, and 50 N (for lubricated sliding) with a reciprocating frequency of 4 Hz and amplitude stroke of 5 mm, and the total sliding distance was 500 m. The 5 wt% zinc-dialkyldithiophosphate (ZDDP) containing mineral-based oil was used as lubricating oil. The lubricating oil was manually dropped (0.5 cc) on the surface after the sample surface reached 100 °C to simulate boundary lubricating condition. The purpose of heating was to provide thermal decomposition of the lubricating oil to form protective tribofilm on the surface. The Al_2O_3 ball (diameter 6 mm) with 16 GPa hardness and 350 GPa elastic modulus was used as a counter body. The main purpose of using an Al_2O_3 ball as the counter body is that both the coating layer and the ball are ceramic materials, and the hardness of Al_2O_3 ceramic balls is adequate for determining the abrasive wear performance of thin hard films [26]. Furthermore, since the alumina ball has a lower hardness than the coatings, it will be worn during the sliding process as a result of the reduced contact area, resulting in a higher level of contact pressure. In addition, alumina is an inert material, therefore any chemical bonding is observed between coating and surface and allowing chemical analyses of the surfaces to be investigated more precisely [27]. The loads were selected to simulate contact pressures exerted on the mold/tool/workpiece interface that was reported to be 2–3.5 GPa. When calculating the load parameter, it was important not to exceed the elastic limit on the first impact and to avoid deformation hardening [28]. The profiles of wear tracks were investigated by a 3D confocal optical profilometer (Zeiss Smartproof-5). After wear tests, the specimens were cleaned ultrasonically with ethanol and acetone solution to achieve worn particle free surface. Following this, the depth and volume of wear scar and wear rate were calculated from recorded data in 3D.

Table 2
Wear test parameters and conditions.

Test parameters	Dry Sliding	Lubricated Sliding
Test type	Reciprocating	
Wear stroke, mm	5	
Sliding speed, mm/s	40	
Sliding Distance, m	500	
Test Duration, min	208.33	
Ball-type	Al_2O_3	
Temperature,∘C	23 ± 2	100 ± 2
Normal load, N	15/20	30/50
Max contact pressure (GPa)		
Bare Steel	1.77/1.95	2.23/2.64
Nitrided	1.81/1.99	2.28/2.70
Coating-A	2.16/2.87	2.72/3.22
Coating-B	2.15/2.36	2.71/3.21
Coating-C	2.21/2.43	2.79/3.30
Coating-D	2.24/2.47	2.83/3.35
Minimum oil thickness (nm)		
Bare Steel	–	51.68/49.78
Nitrided	–	51.49/49.60
Coating-A	–	49.91/48.09
Coating-B	–	49.96/48.13
Coating-C	–	49.92/48.17
Coating-D	–	49.94/48.24
Lambda ratio (λ)		
Bare Steel		0.14/0.14
Nitrided	–	0.14/0.14
Coating-A	–	0.14/0.13
Coating-B	–	0.14/0.13
Coating-C	–	0.14/0.13
Coating-D		0.14/0.13

The wear volumes (V) of specimens were calculated according to Eq. (1):

$$V = 2\pi \times r \times w \times d \tag{1}$$

Where r was the wear track radius; w was the track width; d was the track depth. The wear rate was determined by Archard's wear rate formula Eq. (2) [29]:

$$WR\left(\frac{mm^3}{Nm}\right) = \frac{\text{Wear volume } (mm^3)}{Normal\ load\ (N) \times Wear\ distance\ (m)} \tag{2}$$

Hertzian contact pressures were calculated by using Eq. (3), where E' is the effective modulus, L is the normal load and R is the ball radius [30]. Moreover, the minimum film thickness and Lambda ratios for the boundary lubricated conditions given in Table 2 were calculated by Eqs. (4) and (5), [31]. *(L: load, E': effective elastic moduli, R: diameter of the ball, R_{qb} = root mean square roughness of the ball, R_{qs}: root mean square roughness of the flat sample, U: sliding speed, α: viscosity coefficient = $1.56x10^{-8}$ m^2/N, η_0: dynamic viscosity = $4.96x10^{-3}$ Pa s at 100 °C)* The calculated Lambda values (λ) < 1 states that the boundary lubrication regime was formed for all test conditions [32,33]. For each different normal load, three tests were carried out and the average value was determined.

$$P_{max} = \frac{1}{\pi}\left(\frac{6xLxE'^2}{R^2}\right)^{1/3} \tag{3}$$

$$h_{min} = \frac{2.65 \times \alpha^{0.54} \times (\eta_0 \times U)^{0.7} \times R^{0.43}}{E'^{0.03} \times L^{0.13}} \tag{4}$$

$$\lambda_{min} = \frac{h_{min}}{\left(R_{qb}^2 + R_{qs}^2\right)^{1/2}} \tag{5}$$

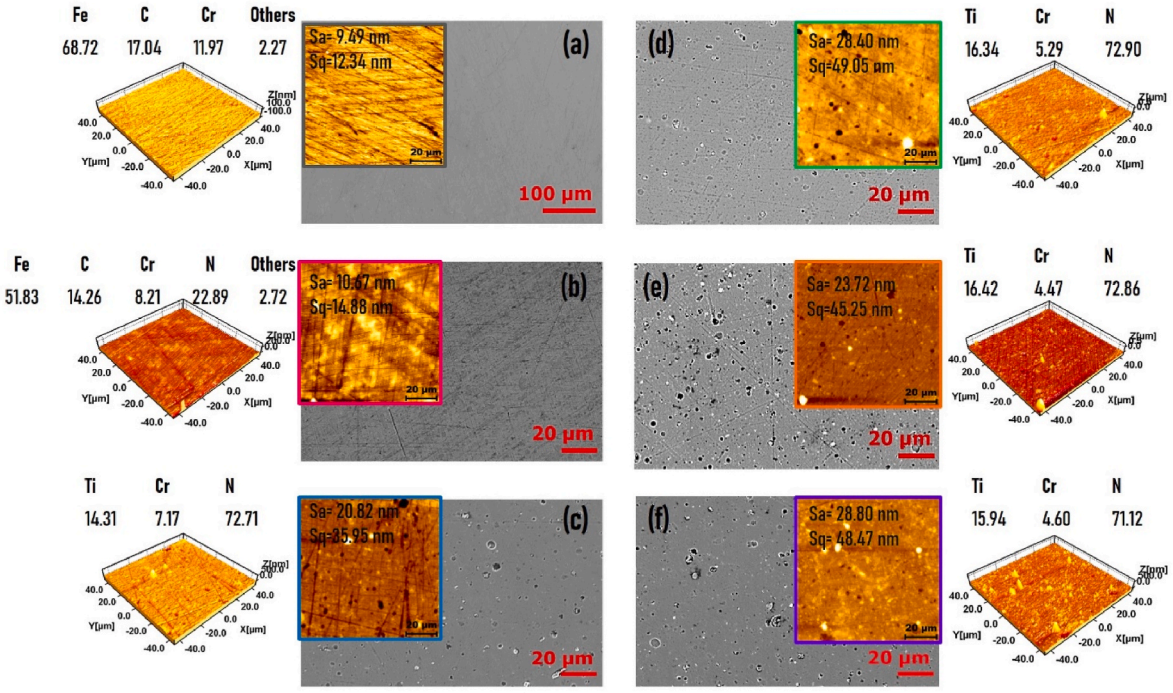

Fig. 2. SEM and AFM images, roughness values and chemical composition of the coating surfaces, (a) Bare steel, (b) Nitrided steel (c) Coating A, (d) Coating B, (e) Coating C, (f) Coating D.

3. Results

3.1. Microstructure and morphology of the coatings

The surface roughness of substrate is an important parameter in influencing the adhesion between the substrate and the coating. The interfacial stress, deformation tendency and direction of crack propagation are related to roughness [34,35]. The SEM and AFM were used to analyze the surface morphology of the coatings and EDX was also used to investigate the chemical properties of the coating surfaces. The arithmetical mean height (Sa) and root mean square height (Sq) values for the coatings were shown in Fig. 2. The Sa/Sq values (±5 nm) of coatings A and B were 20.82/35.95 nm and 28.40/49.05 nm, whereas the roughness values of coatings C and D were found to be 23.72/45.25 nm to 28.20/48.47 nm, respectively.

It was found that the coated specimens have rougher surface and show micro droplets known as molten cathode particles (pointed by the blue arrows), which were seen on the SEM and AFM images. The droplets on the surface increase surface roughness and play role as abrasive particles under high load [36]. The coatings deposited on nitrided samples have higher surface roughness for both coating architectures. The increased surface roughness following duplex treatment could be explained by the Volmer-Weber growth mode which indicated that ion groups preferentially nucleate at defects formed during the nitriding process [37].

The Ti/N ratio is a crucial component that influences not only the stoichiometry of the coating but also its structure and mechanical characteristics. The nitride composition is obtained with a large quantity of nitrogen transmitted on the vacuum chamber, and stoichiometric structure is difficult at a reasonably high nitrogen flow and high pressure in the chamber. Assuming that the plasma plume contains roughly equal amounts of titanium and nitrogen, titanium tends to be situated deeper inside the coating due to its heavier nature, whilst nitrogen tends to congregate closer to the coating's surface. When the coatings are thicker, there is a wider vacancy between titanium and nitrogen accumulation zones, therefore areas that close to the surface are nitrogen-rich [38]. Therefore, the quantity of Ti and N indicated that all coatings' surfaces consisted of a composition of non-stoichiometric. When investigating the coating SEM/EDX results, similar surface composition was seen for all coating types. The average Ti/N stoichiometries were determined as 26 and 33% for coatings A-B, and C-D, respectively. According to the literature, the over-stoichiometry for TiN is predictable due to the different diffusion rates of Ti and N [39].

The coating thickness was determined by SEM and Calotest analyses. The cross-section analyses of coatings were presented in Fig. 3 and

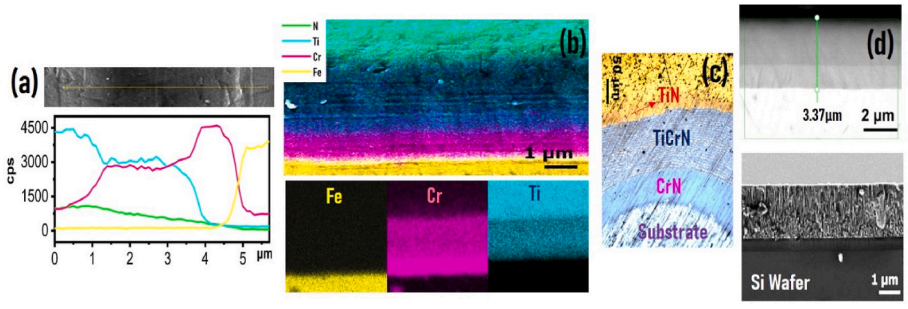

Fig. 3. a) EDX line graph, b) EDX mapping image, c) Calotest optic microscope images, d) SEM cross section image of Si wafer and specimens for Coating A and B.

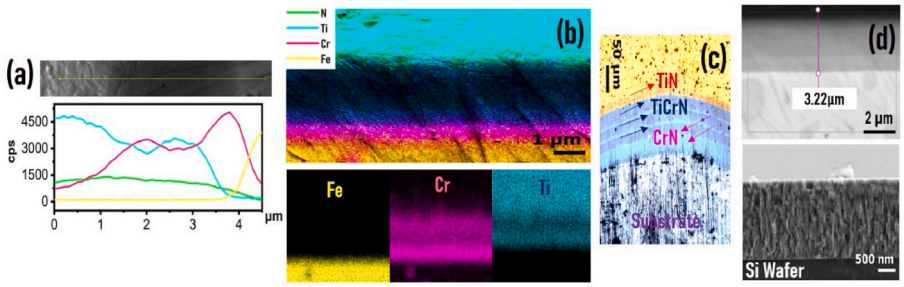

Fig. 4. a) EDX line graph, b) EDX mapping image, c) Calotest optic microscope images, d) SEM cross section image of Si wafer and specimens for Coating C and D.

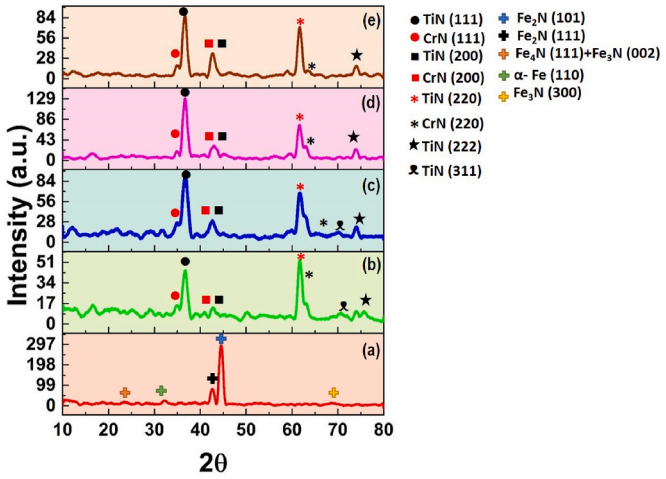

Fig. 5. XRD analysis of the specimens, (a) Nitrided, (b) Coating A, (c) Coating B, (d) Coating C, (e) Coating D.

Fig. 4. The coating thickness is directly related to the quantity of the evaporated material, deposition time, chemistry properties of the nitrogen compound, and the parameters of transporting target material on the substrate [40]. To explore the microstructure of coatings, a cross-sectional SEM image of the coated Si (100) wafer and steel substrates was provided in Figs. 3 and 4. Because of the ion bombardment induced by the high nucleation rate of cathodic arc processes, all coatings have an intense columnar structure. Additionally, the SEM images revealed that the interlayers were tightly attached to the substrate and that the coating was successfully deposited, with no delamination or porosity within the coatings or at the substrate-coating interface. The coatings' strong adhesion properties could be attributed to the solid solution formed by the Ti and Cr ions, which form a significant interlock. Moreover, Fig. 3 and Fig. 4show the chemical composition of coating layers explored by using the EDX line scan and cross-sectional mapping. The EDX measurements were consistent with the chemical composition of the deposited TiN/TiCrN coating structure. In addition, the coating layers and CrN interlayers were clearly shown in the optical microscope images of the Calotest analysis. The thickness of the TiN/TiCrN coating without CrN interlayer was found to be 3.37 and 3.06 μm for coating A and B, respectively. The thickness of the TiN/TiCrN coating with two CrN interlayer were determined to be 3.22 and 3.13 μm for coating C and D, respectively.

The crystalline structure of the coatings was investigated by XRD analyses. The XRD patterns of coatings were shown in Fig. 5. The (111), (200) and (220) diffraction planes of all coated specimens were observed at a diffraction angle (2θ values) of standard TiN (JCPDS No. 87–0633) and CrN (JCPDS No. 77-0047) [36]. The 2θ values of

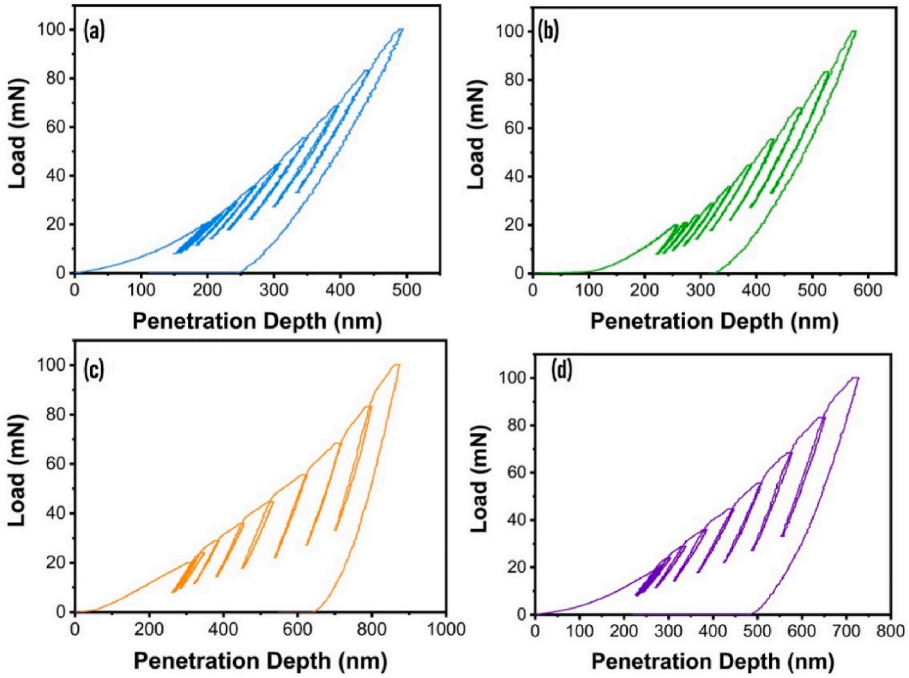

Fig. 6. Load-displacement curves of the coated specimens, (a) Coating A, (b) Coating B, (c) Coating C, (d) Coating D.

Table 3
Mechanical properties and crystallite sizes of the specimens.

Sample	Hardness (±3 GPa)	Elastic modulus (±3 GPa)	H/E	H^3/E^2 (GPa)	Coating thickness (±0.1 μm)	Average Crystallite sizes (±2 nm)
Bare Steel	7.43	190.33	0.03	0.01	–	–
Nitrided	9.45	202.04	0.04	0.02	–	–
Coating A	27.32	320.94	0.08	0.19	3.37	7.96
Coating B	25.16	316.57	0.07	0.15	3.06	6.38
Coating C	29.42	345.18	0.08	0.21	3.22	7.87
Coating D	32.58	360.15	0.09	0.26	3.13	7.92

diffraction peaks of coatings were about 2θ = 36–38° (111), 2θ = 42–44° (220), 2θ = 61–63° (200), 2θ = 74–76° (222), respectively. According to this finding, the as-deposited thin films created a solid solution between themselves by substituting the host metal atoms. The solid solution for TiCrN coatings could be depicted as Cr atoms in the CrN structure being subrogated by Ti atoms [41]. The coatings' lattice constants increased because the radius of the Ti atom (1.445 Å) is larger than the radius of the Cr atom (1.249 Å) due to the Cr atom being replaced with the Ti atom in the CrN structure [42]. Furthermore, as the number of layers increased, the crystal orientation for the TiCrN films changed from (111) to (200). The dominant diffraction peak obtained for (111) could be assigned to the FCC B1 structure, which has the lowest strain energy [43]. The wide range of XRD peak widths indicates that the coatings were highly crystalline structure. The coatings' crystallite sizes were determined to be about 6–8 nm, indicating that the TiCrN were anostructured coatings (Table 2). At time same time, XRD analysis of the duplex-treated samples did not show any FexN peaks due to the grazing incidence method used. It should be noted that XRD analysis can only provide average structural information of a much thinner coating layer (less than 4 μm) compared to the compound layer. Additionally, the iron nitride phases may decompose during the Cr ion bombardment, especially by high-energy ions [44].

In addition to the primary ferrite phase, low-intensity peaks of the ε-Fe_3N and γ-Fe_4N phases creating the white layer were evaluated in the nitrided sample. The interactions between N and Fe (in larger percentages in the compound layer) formed iron nitrides, which enhanced mechanical properties. Nevertheless, the presence of unstable ε-Fe_3N and γ-Fe_4N phases in the white layer produced a brittle structure that was undesirable in forming operations [45,46]. The characterization of current phases in the compound layer is critical since each phase has a particular function in affecting material characteristics. The production of γ-Fe_4N is associated with poor cooling rates because this phase precipitates throughout the cooling process and cannot be spotted by SEM [47].

3.2. Mechanical properties of the coatings

Both hardness and elastic modulus of the coatings were calculated by the indenter tests. Indentation loading curves corresponding to the coated specimens were shown in Fig. 6. Considering the multi-layered architecture of the coating, loading curves were shown at different penetration depths. However, as the depth of penetration increases, the hardness and elastic modulus tend to decrease due to the influence of the deformation properties of the substrate material. For this reason, the results at 300 nm penetration depth were considered as a reference in determining the mechanical properties of the coatings. As shown in the load-displacement curves, the penetration depth is approximately 300 nm which is smaller than 10% of the coating thickness.

Coating B had the lowest elastic modulus and hardness of 316.5/25.16 GPa, whereas coating D had the highest elastic modulus and hardness of 360.1/32.58 GPa (see Table 3). Moreover, the ratio H/E exhibits the elastic strain to failure and H^3/E^2 the resistance to plastic deformation. Coatings with close H/E and H^3/E^2 ratios shown excellent wear resistance at the wear tests [48]. The H^3/E^2 ratio has the lowest value of 0.15 for coating B and the highest value of 0.26 for coating D. Additionally, the Hall-Petch model depends on dislocation motion within layers and across layer interfaces, has been successfully used to multilayers to explain this hardness improvement. It is possible to apply the Hall-Petch effect when the ceramic materials like hard multilayer coatings with are higher than that of 5.2 nm. According to the Hall-Petch equation, an increase in hardness can be explained by the grain size of the coatings, since smaller grains result in higher grain boundaries density and therefore there are more barriers to dislocations, resulting in an increase in hardness with decreasing grain size [49].

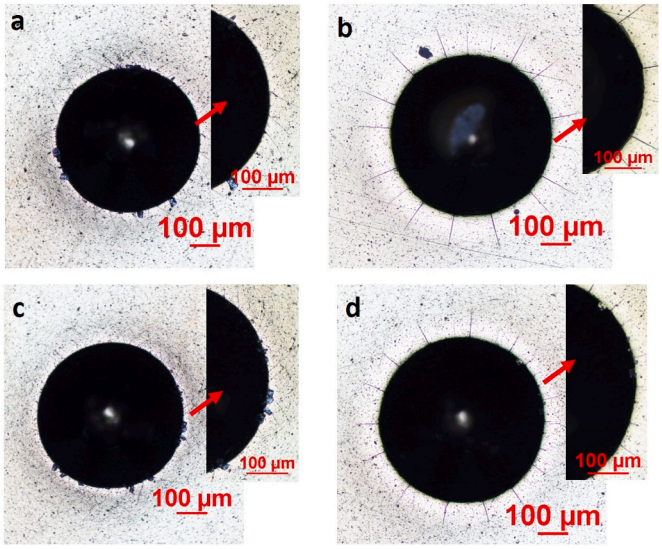

Fig. 7. Optical microscope images of Rockwell-C indentation of the (a) Coating A, (b) Coating B, (c) Coating C, (d) Coating D.

The Rockwell C indenter images of coatings were exhibited in Fig. 7. Adhesion is one of the most important parameter of coating/substrate durability since it influences the coating's strength and effective life [50]. The adhesion levels of coatings were determined as HF1 for Coating A, HF2 for Coating B, HF1 for Coating C, and HF2 for Coating D. Moreover, small size cracks known as the eggshell effect were observed in the Rockwell C indentation of the nitrided samples (Coating B and D). Although the nitriding zone can function as an interfacial transition zone, the presence of γ-Fe4N or - ε-Fe2,3 N compounds in the nitrided layer reduce adhesion and result in "eggshell failure." This hard and brittle compound layer, where fractures tend to produce and propagate, explains why the coating's adhesion and loading capacity are reduced [37]. Compressive stress cracks developed and spallation occurred at the indentation edge when the coating was too stiff for plastic deformation. Nonetheless, this crack level surrounding the indentation was acceptable because there was no layer delamination on the coating surfaces in this work. Choosing the appropriate interlayers and adhesion layer that complement the deposited coating type ensures a dense coating structure and is therefore an important step in developing strong adhesion [51]. Although the four coating types exhibited similar mechanisms of abrasive and adhesive wear due to their high hardness and ductility under dry conditions, adhesion and columnar morphology had a significant impact on their wear behavior. Moreover, a non-porous and dense coating structure was found to provide strong adhesion at the HF1-HF2 level [52]. Despite its columnar growth, the coating may develop large cracks or fractures under high loads or contact pressures in lubricating conditions, especially in weaker adhesion areas or along

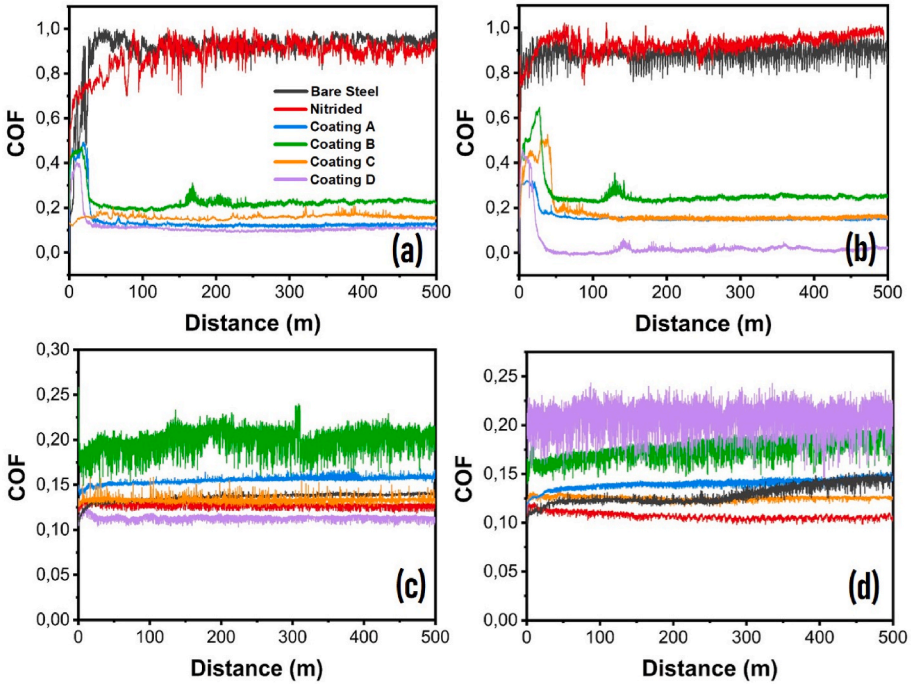

Fig. 8. COFs of the coatings, (a) at 15 N dry conditions, (b) at 20 N dry conditions, (c) at 30 N lubricated conditions, (d) at 50 N lubricated conditions.

columnar grain boundaries, resulting in reduced wear performance [53].

3.3. Friction and wear properties

Fig. 8 shows the friction coefficients (COFs) versus sliding distance for all samples under normal loads of 15/20 N and 30/50 N for dry and lubricated conditions, respectively. The bare steel and nitrided sample had the highest COF of approximately 0.90 at both 15 N and 20 N loads under dry condition. The coatings showed similar behaviour in COFs trends at the dry condition, i.e. curves increased sharply to 0.4 at the beginning and reached a steady-state friction regime after 50 m sliding distance. The short running-in period with high and unstable COF resulted from breakage of TiN top layer as well as the initial wear of the surfaces' micro asperities. In this way, brittle micro-fractures within surface grains can promote wear damage in the initial stage [54]. However, after the TiN layer removed from surface, coated specimens exhibited a steady-state low friction regime and superior wear resistance when sliding under dry condition because of the formation of lubricious thin tribo-films consist of Magnéli phases such as chromium oxides [55]. On the other hand, TiN/TiCrN coatings showed different COFs and trends at 20 N (Fig. 8 (b)). Different fluctuation patterns showing the breakdown of the interlayers were noticed before reaching the steady-state friction regime when investigating at the COFs curves of the

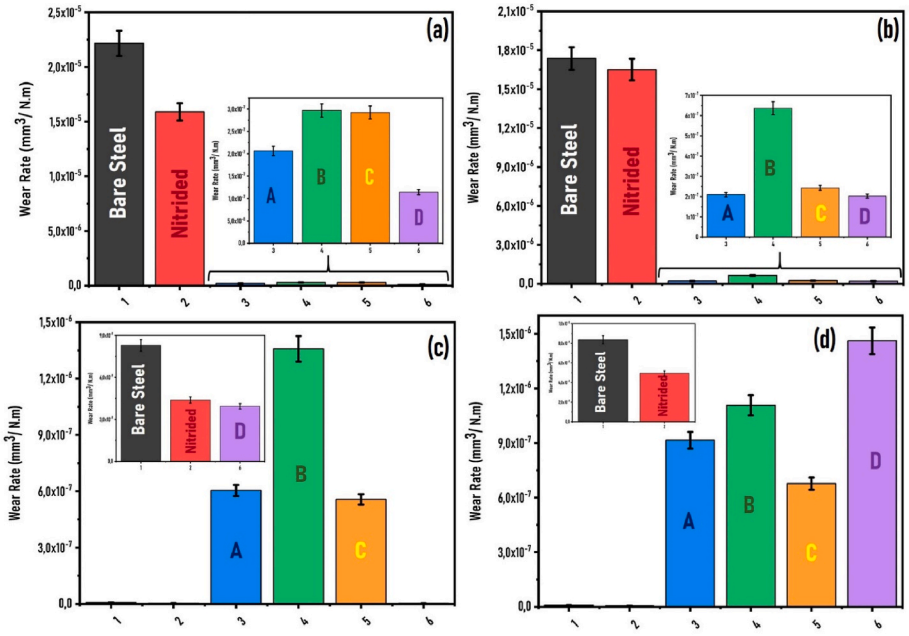

Fig. 9. Wear rates of the coatings at a) at 15 N dry conditions, (b) at 20 N dry conditions, c) at 30 N lubricated conditions and (d) at 50 N lubricated conditions.

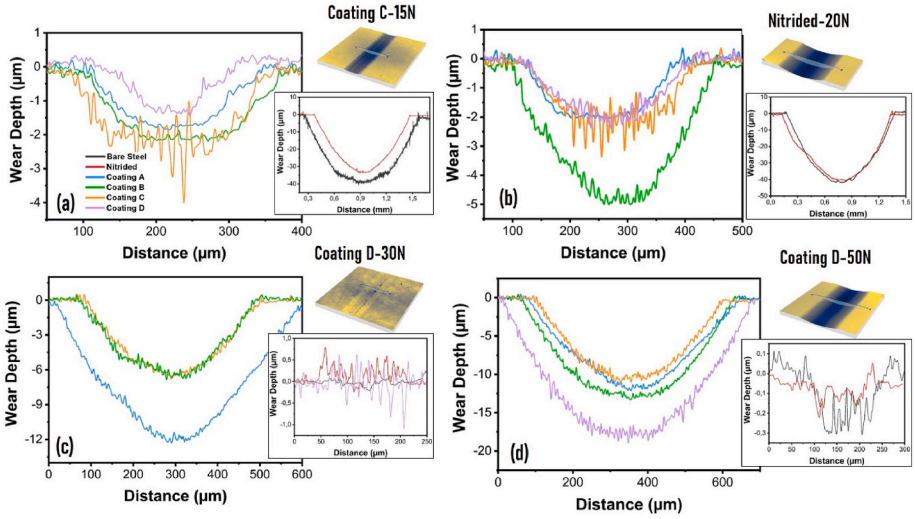

Fig. 10. Wear depth graphs of the coatings at a) at 15 N dry conditions, (b) at 20 N dry conditions, c) at 30 N lubricated conditions and (d) at 50 N lubricated conditions.

coatings tested at 20 N. According to the COF curves, coated samples achieved steady-state COFs (about 0.19 for Coating A and C, 0.30 for Coating C and 0.04 coating D). This indicated that coating D had the best wear resistance along with only top TiN layer break down when compared to other coatings. Furthermore, the COF curves of the bare and nitrided samples both increased to a steady value of 0.9 at 15 N after more longer run-in period at dry condition (see Fig. 8(a)). However, the COF value of the bare and nitrided sample showed no difference as the normal load increases, as shown Fig. 8(b). This behavior is predicted in nitrided steels with a hard ceramic layer, or white layer, composed of –$Fe_{2,3}N$ and -Fe_4N brittle phases. Fig. 8 (c and d) shows the evolution of friction in lubricated condition. Except for coating A and B, all specimens had approximately 0.12–0.14 COF values lower than dry condition. Coating D had the lowest COF of 0.11 when compared to other coatings. Coating A and B was excluded from this general evaluation and demonstrated a rather high COF value of 0.15 and 0.19, respectively. Coating A had a high COF following coating B, and the wear rate of this coating in Fig. 9 supported this conclusion. According to the COF curves, ZDDP provided poor wear protection for coatings A and B, which could be attributed to high Hertzian contact pressure of 2.72 GPa and surface roughness [56]. In the test performed at 50 N load, the coating D had the highest COF value of 0.20, unlike the value at 30 N load. This indicates that the COF values of the coatings change depending on the load under lubricated conditions and there was a load threshold value. The lubrication film thickness (~48 nm) formed on the sliding surfaces by the ZDDP-containing lubricant was close to the surface roughness of coatings (~35–48 nm), therefore the lubrication effect decreases during wear test. Load is imparted to these asperities during contact, and the load is carried by the fewest number of contact points, exposing these locations to significant local stress. It can be concluded that ZDDP lubrication film was insufficient for enhancing the wear characteristics of coatings A, B, C and D, and intensive abrasive wear scar were obtained due to large surface peaks [57–59].

The wear rate and depth profiles of specimens were shown in Figs. 9 and 10, respectively. For 15 N, coatings A, B and C had similar and highest wear rates of 2.06×10^{-7} mm^3/N.m, 2.96×10^{-7} mm^3/N.m and 2.92×10^{-7} mm^3/N.m, respectively, however; wear rate of coating D is 1.4×10^{-7} mm^3/N.m (see Fig. 9). The results confirmed the positive

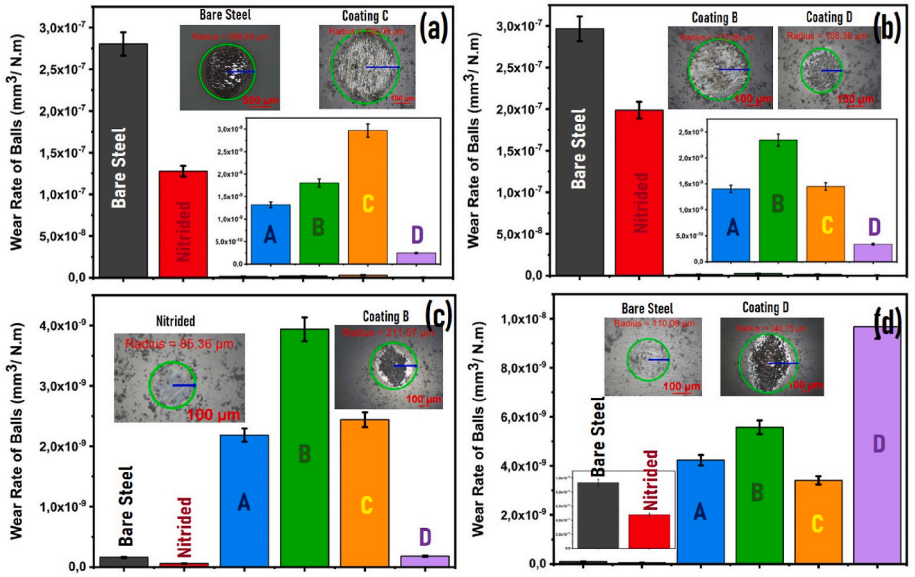

Fig. 11. Wear rate of alumina balls at a) at 15 N dry conditions, (b) at 20 N dry conditions, c) at 30 N lubricated conditions and (d) at 50 N lubricated conditions.

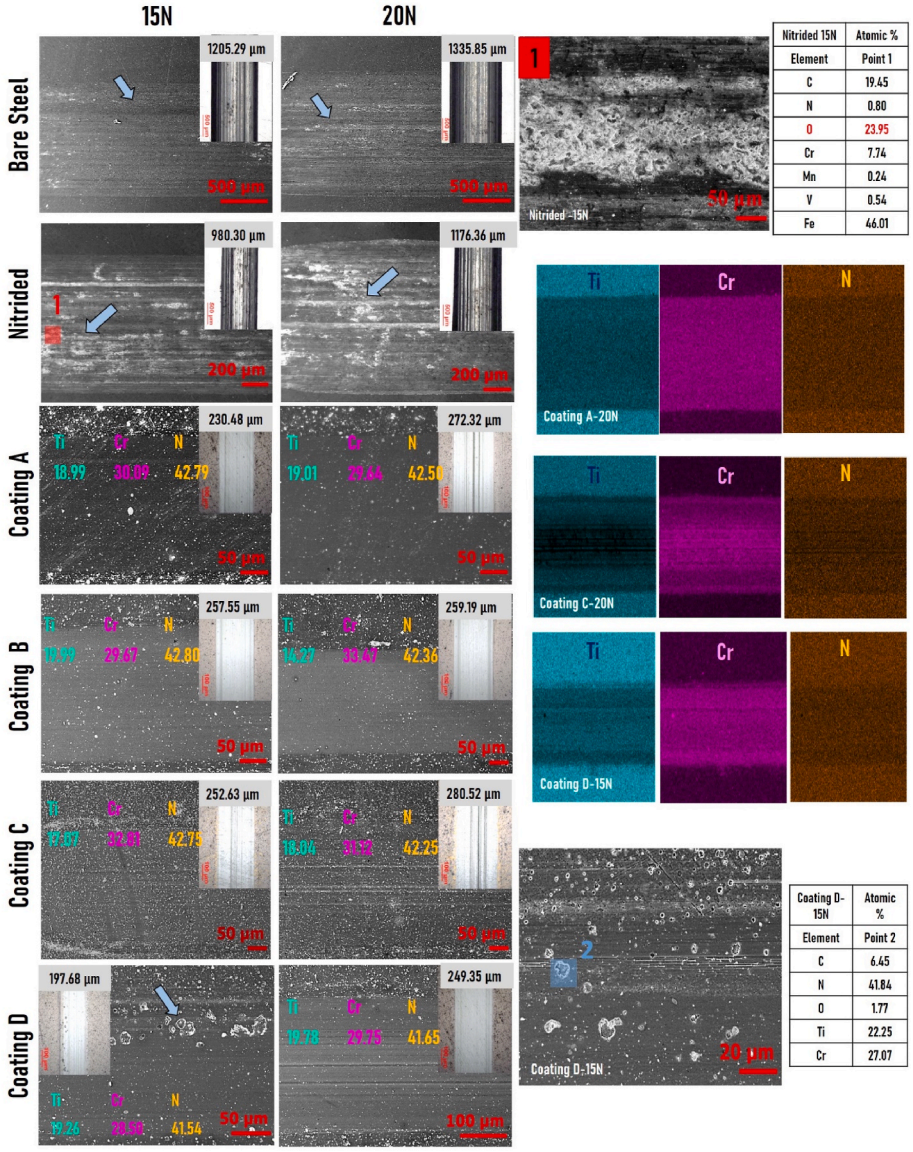

Fig. 12. SEM and optic microscope images wear scars and EDX analysis of the coating A/B/C/D and bare/nitrided sample at 15 N and 20 N dry conditions.

effect on the load-bearing capacity of the nitriding layer for the dry condition. Although the low wear rates of coated specimens, bare steel have the greatest wear rate of 2.21×10^{-5} mm^3/N.m and nitrided steel having the second highest wear rate of 1.58×10^{-5} mm^3/N.m at 15 N. For 20 N, the coating B had the highest wear rate of 6.36×10^{-7} mm^3/N.m, whereas the coatings A, C and D had wear rates of 2.09 × 10-7 mm^3/N.m, 2.42×10^{-7} mm^3/N.m, and 2.02×10^{-7} mm^3/N.m, respectively. As with the wear rates at 15 N load, bare steel and the nitrided sample have the highest wear rates of and 1.73×10^{-5} mm^3/N.m and 1.65×10^{-5} mm^3/N.m, respectively. In Fig. 9 it is clearly seen that wear resistance of coating B decrease due to lower hardness value.

The wear rate calculations were validated by typical cross-sectional linear profiles of the wear scars, as illustrated in Fig. 10. Coating D exhibited the lowest wear depth of 1.57 µm at 15 N and 2.10 µm at 20 N. Additionally, the wear depth for bare and nitrided steel were approximately between 35 and 40 µm under dry sliding conditions.

For 30 N, coating D had the lowest wear rate of 3.93×10^{-9} mm^3/N.m besides bare steel and nitrided sample, while coating B had the highest wear rate of 1.35×10^{-6} mm^3/N.m. On the other hand, wear rate of samples at 50 N was examined, coated specimens attracted attention due to their high wear rate when compared to bare and nitrided samples. Coating D had the highest wear rate of 1.46×10^{-6} mm^3/N.m and the highest wear depth of 18.09 µm (Fig. 10). In addition, abrasive scars on the worn surface of the coating were more noticeable under the lubricated condition as compared to the unlubricated condition. Wear rates revealed that the wear resistance of the coatings decreased significantly at the lubricated conditions. Another notable result was nitriding steel's enhanced anti-wear performance under lubricated conditions. Particularly for 50 N, the nitrided sample had the lowest wear rate of 4.94×10^{-9} mm^3/N.m and the lowest wear depth (0.21 µm) compared to unlubricated conditions. This could be explained by the formation of a lubrication film between the ball and the nitrided sample with low surface roughness, which significantly decreased wear during the wear test [57]. Additionally, Ito et al. found that if an iron oxide (Fe_3O_4) layer was present, ZDDP molecules in the lubricant would degrade, releasing free zinc ions at 60 °C. These free ions could then adhere to the iron oxide surface, generating a zinc-rich, sulphur-free absorption layer ($ZnFe_2O_4$) [60]. At the same time, this anti-wear performance is linked to nitrogen diffusion and the creation of hard nitrided surfaces at the bare steel surface [45].

The comparison of ball wear rates was illustrated in Fig. 11 and wear rates of balls were found to be similar to wear rates of coatings, there is a

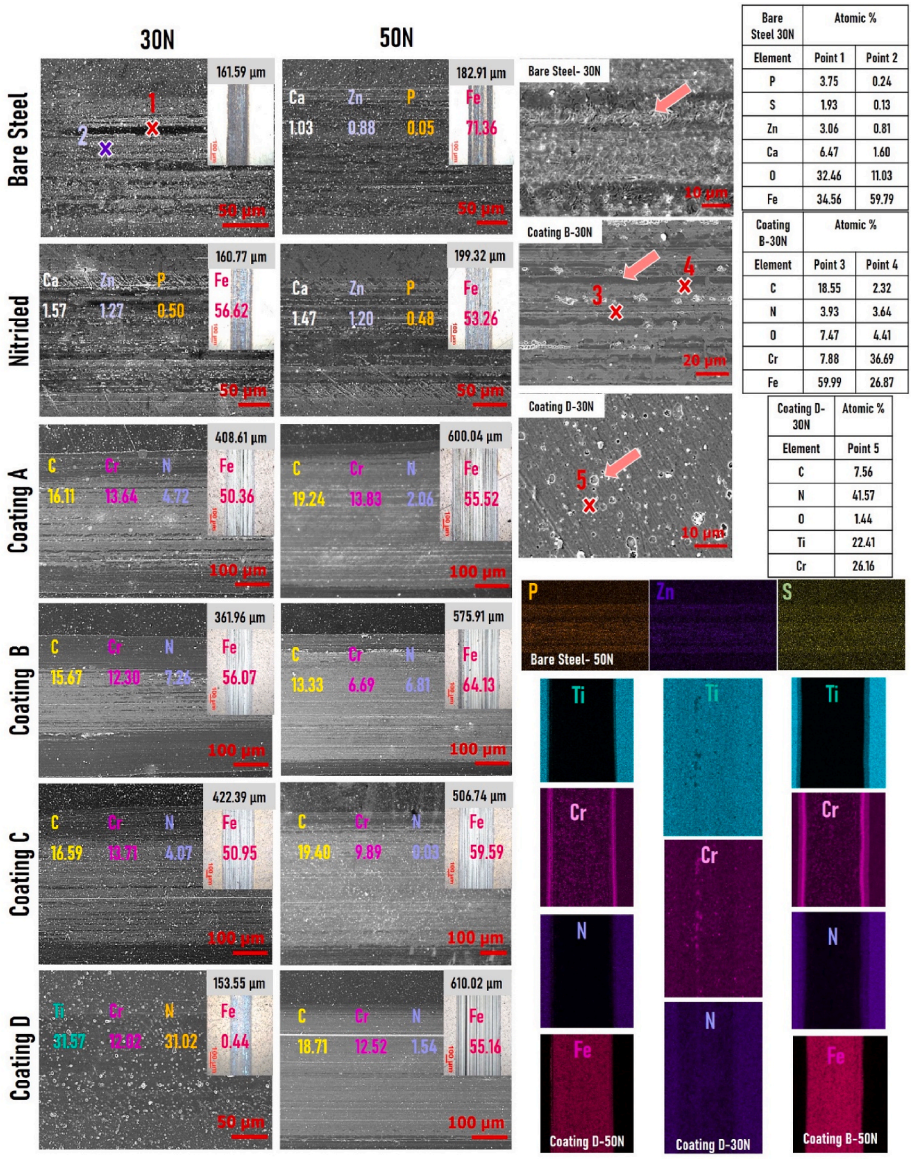

Bare Steel 30N	Atomic %	
Element	Point 1	Point 2
P	3.75	0.24
S	1.93	0.13
Zn	3.06	0.81
Ca	6.47	1.60
O	32.46	11.03
Fe	34.56	59.79

Coating B-30N	Atomic %	
Element	Point 3	Point 4
C	18.55	2.32
N	3.93	3.64
O	7.47	4.41
Cr	7.88	36.69
Fe	59.99	26.87

Coating D-30N	Atomic %
Element	Point 5
C	7.56
N	41.57
O	1.44
Ti	22.41
Cr	26.16

Fig. 13. SEM and optic microscope images wear scars and EDX analysis of the coating A/B/C/D and bare/nitrided sample at 30 N and 50 N lubricated conditions.

clear linear relationship between wear scar width and worn area. The wear rates of the alumina balls of the coated samples are lower than the bare steel and nitrided samples at dry condition. Furthermore, EDS analyses of wear scars confirmed material transfer from the coating to their counterfaces and suggested possible tribochemical reactions. When examining the lubricated conditions, a significant wear scar width and ball-worn area radius increase were obtained for all coatings except Coating D at 30 N. In contrast to dry conditions, the highest ball worn area radius (348.7 μm) was obtained for coating D at 50 N.

3.4. Tribochemical analysis of the wear scar

SEM and optical microscope images, EDX mapping analysis of the coatings at 15 N and 20 N dry conditions were shown in Fig. 12. Wear scar widths at 15 N and 20 N for bare steel and nitrided samples were 1205/980 μm and 1335/1176 μm, respectively. The SEM and optical microscope images demonstrated more intensive abrasive and adhesive wear on the surface of the bare and nitrided steel than coated samples, whereas adhesive wear was observed on balls that ran against these materials. Furthermore, the lowest wear scar width was 197 μm for coating D, and similar wear scar widths were achieved for other coatings. The high amount of oxygen and iron element ratio in the results of EDX analysis no. 1 performed in the wear scar at 15 N load of the nitrided sample showed that the nitriding layer could not provide an effective protection barrier and caused oxidative wear.

The improved hardness and toughness provided by the coating process reduced the width and depth of wear scars. The coated samples have shown significant enhancement in wear resistance and the SEM/EDX results confirmed the wear analysis results because of coated specimens had coating elements on worn surface. Besides, the presence of Cr elements in the EDX of coated sample showed that the TiN top layer had been fractured and that wear depth had reached CrN or TiCrN interlayers during the wear tests. It was determined by EDX analysis that the particles marked with the number 2 in the SEM images of coating D belong to the coating.

SEM and optical microscope images, EDX mapping analysis of the coatings at 30 N and 50 N lubricated conditions were shown in Fig. 13. When the wear scars were considered under the lubricated conditions, the bare/nitrided samples showed a considerable reduction in wear scar widths. However, unlike the dry friction condition, there was a large increase in the wear scar widths of the coated samples, except for Coating D (153 μm), at 30 N load. The SEM/EDX analysis results were

similar to wear rate and demonstrated the poor antiwear behavior for coatings at lubricated conditions. Coating C and D had the widest wear scar for 30 N (422 μm) and 50 N (610 μm) in comparison to unlubricated conditions. In addition, under 50 N lubricated conditions, the wear scars of the coating D showed significant abrasive wear (see Fig. 12) [61,62]. Lubrication film formation could not be achieved because the minimum film thickness was close to the high surface roughness value caused by the droplets formed on the surface during the coating process. For this reason, the wear particles detached from the surface peak points cause a deeper scraping effect in this sample with the third body effect. Further, the particles from the TiCrN coatings transferred and adhered to the surface of the Al_2O_3 ball as more wear material moved to the alumina ball surface sliding against coating D, which has the highest wear rate (see Fig. 9). The higher level of Fe, C and Cr detection in the wear scars of coated specimens at 50 N was the evidence of reaching the substrate material which means that higher wear rate.

However, the strong lubrication film formation could be seen in SEM and optical images, particularly for bare and nitrided samples, instead of abrasive wear lines located at dry conditions. For bare steel and nitrided spesimens, detected Zn, P, Ca were originated from the thermal degradation of the ZDDP antiwear additive during sliding. SEM/EDX results revealed that coating D had the lowest wear resistance for the lubricated conditions at 30 N, despite the fact that no components of the lubrication materials were found on the wear scar surface. Because the presence of Ti, Cr and N elements belonging to the coating in the wear trace of the coating D were clearly seen in the mapping analysis and showed that although a lubricating film is not formed, the coating D improves wear resistance up to a certain load level.

4. Conclusion

In this study, the TiN/TiCrN coatings with different architecture were deposited on nitrided and non-nitrided DIN 1.2379 work steel specimens using cathodic arc-PVD. The crystal structure, atomic content of elements, nanohardness, adhesion strength and wear performance of coatings were investigated to explore the nitriding effect on tribological behavior ay dry and lubricated conditions. All coatings were deposited on the nitride and non-nitride steels in columnar structure with higher level density. The results showed that all coatings significantly improved the wear resistance and surface hardness of DIN 1.2379 work steel for dry sliding conditions and the coating D showed the lowest COF of 0.12 and 0.04 at 15 N and 20 N, respectively. Higher friction coefficients with larger fluctuation and higher wear rate were observed in bare and nitrided steel at dry condition. For the lubricated conditions, coating D and nitrided steel showed the lowest COF of 0.12 and 0.13 at 30 N. However, the high wear scar depth and low wear resistance obtained in the coating D at 50 N were due to the high surface roughness. The fact that the coating D has the lowest wear resistance at 50 N load is due to the fact that the hard particles contained in the CrN interlayer and nitriding layer accelerate the wear. Additionally, the results revealed that a relatively hard and thick CrN interlayer on nitrided layer can improve the adhesion of the TiN/TiCrN coating by reducing plastic deformation of the substrate at dry conditions. Meanwhile, oxide phases that formed on wear scar surface such as chromium oxide have been reported to best wear resistance for dry sliding condition. Accompanied by these results, combining of nitriding and TiN/TiCrN coating is promising candidate for improving the performance of mold and tool applications.

Declaration of competing interest

The authors declare that they have no known competing financial interests or personal relationships that could have appeared to influence the work reported in this paper.

Data availability

Data will be made available on request.

Acknowledgment

The authors would like to thank Titanit Ultra Hard Coating company for coating applications, and Koç University Surface Science and Technology Center for XRD analyses and Sabancı University Nanotechnology Research and Application Center for SEM/EDX analyses and other providing the necessary facilities and resources for this research.

References

[1] K. Holmberg, A. Erdemir, Influence of tribology on global energy consumption, costs and emissions, Friction 5 (2017) 263–284, https://doi.org/10.1007/s40544-017-0183-5.
[2] P. Mayrhofer, R. Rachbauer, D. Holec, F. Rovere, J. Schneider, Protective transition metal nitride coatings, Comprehen. Mater. Proces. 4 (2014) 355–388, https://doi.org/10.1016/B978-0-08-096532-1.00423-4.
[3] H.K. Tönshoff, A. Mohlfeld, PVD-Coatings for wear protection in dry cutting operations, Surf. Coating. Technol. 93 (Issue 1) (1997) 88–92, https://doi.org/10.1016/S0257-8972(97)00027-3.
[4] M. Khadem, O.V. Penkov, H.K. Yang, D.E. Kim, Tribology of multilayer coatings for wear reduction: a review, Friction 5 (2017) 248–262, https://doi.org/10.1007/s40544-017-0181-7.
[5] S. Sharifi Malvajerdi, A. Sharifi Malvajerdi, M. Ghanaatshoar, TiCrN-TiAlN-TiAlSiN-TiAlSiCN multi-layers utilized to increase tillage tools useful lifetime, Sci. Rep. 9 (2019), https://doi.org/10.1038/s41598-019-55677-8.
[6] V.P. Tabakov, A.S. Vereschaka, A.A. Vereschaka, Multilayer composition coatings for cutting tools: formation and performance properties, Mech. Indus. 18 (2017) 706, https://doi.org/10.1051/meca/2017063.
[7] A. Pogrebnjak, K. Smyrnova, O. Bondar, Nanocomposite multilayer binary nitride coatings based on transition and refractory metals: structure and properties, Coatings 9 (2019) 55, https://doi.org/10.3390/coatings9030155.
[8] M. Benkahoul, P. Robin, S.C. Gujrathi, L. Martinu, J.E. Klemberg-Sapieha, Microstructure and mechanical properties of Cr–Si–N coatings prepared by pulsed reactive dual magnetron sputtering, Surf. Coating. Technol. 202 (2008) 3975–3980, https://doi.org/10.1016/j.surfcoat.2008.02.014.
[9] Y.H.L. Willey, P.L. Hooi, J.T.M. Gan, D. Jedol, J. Zhong-Tao, Thermal stability, mechanical properties, and tribological performance of TiAlXN coatings: understanding the effects of alloying additions, J. Mater. Res. Technol. 17 (2022) 961–1012, https://doi.org/10.1016/j.jmrt.2022.01.005.
[10] H. Pan, Y. He, X. Zhang, Interactions between dislocations and boundaries during deformation, Materials 14 (2021) 1012, https://doi.org/10.3390/ma14041012.
[11] C. Paksunchai, C.S. Denchitcharoen, S. Chaiyakun, P. Limsuwan, Growth and characterization of nanostructured TiCrN films prepared by DC magnetron cosputtering, J. Nanomater. (2014) 1–9, https://doi.org/10.1155/2014/609482.
[12] M.A. Ezazi, M.M. Quazi, E. Zalnezhad, A.A.D. Sarhan, Enhancing the tribo-mechanical properties of aerospace AL7075-T6 by magnetron-sputtered Ti/TiN, Cr/CrN & TiCr/TiCrN thin film ceramic coatings, Ceram. Int. 40 (2014) 15603–15615, https://doi.org/10.1016/j.ceramint.2014.07.067.
[13] S. Chen, D. Luo, G. Zhao, Guangbin, investigation of the properties of TixCr1-xN coatings prepared by cathodic arc deposition, Phys. Procedia 50 (2013) 163–168, https://doi.org/10.1016/j.phpro.2013.11.027.
[14] F.F. Komarov, O.D. Pohrebniak, S.V. Konstantinov, Formation and characterization of nanostructured composite coatings based on the TiN phase, Acta Phys. Pol. 125 (2014) 1292–1295.
[15] Y.X. Ou, J. Lin, S. Tong, H.L. Che, W.D. Sproul, M.K. Lei, Wear and corrosion resistance of CrN/TiN superlattice coatings deposited by a combined deep oscillation magnetron sputtering and pulsed dc magnetron sputtering, Appl. Surf. Sci. 351 (2015) 332–343, https://doi.org/10.1016/j.apsusc.2015.05.110.
[16] D.E. Wolfe, B.M. Gabriel, M.W. Reedy, Nanolayer (Ti,Cr)N coatings for hard particle erosion resistance, Surf. Coating. Technol. 205 (2011) 4569–4576, https://doi.org/10.1016/j.surfcoat.2011.03.121.
[17] A.F. Rousseau, J.G. Partridge, E.L.H. Mayes, J.T. Toton, M. Kracica, D. G. McCulloch, E.D. Doyle, Microstructural and tribological characterisation of a nitriding/TiAlN PVD coating duplex treatment applied to M2 High Speed Steel tools, Surf. Coating. Technol. 272 (2015) 403–408, https://doi.org/10.1016/j.surfcoat.2015.03.034.
[18] A. Ballesteros-Arguello, F.O. Ramírez-Reyna, G.A. Rodríguez-Castro, A. Meneses-Amador, D. Fernández-Valdés, O. Reyes-Carcaño, Experimental and numerical evaluation of the contact fatigue resistance of AlCrN, FexN and AlCrN/FexN coatings on AISI 4140 steel, Surf. Coating. Technol. (2021) 423, https://doi.org/10.1016/j.surfcoat.2021.127620.
[19] K. Holmberg, A. Matthews, Chapter 4 Tribological Properties of Coatings, Tribology Series, vol. 28, Elsevier, 1994, pp. 125–256, https://doi.org/10.1016/S0167-8922(08)70754-5.
[20] B. Pina, H.N. Shah, Morphological analysis of nitride coated steel for industrial application, Trends Mech. Eng. Technol. 6 (2016).

[21] D. Amari, H. Khireddine, Y. Khelfaoui, N. Saoula, Adhesion and corrosion of Ti, TiN and TiCrN films deposits on AISI 316L in SBF solution, Defect Diffusion Forum 397 (2019) 39–50. https://doi.org/10.4028/www.scientific.net/ddf.397.39.
[22] S. Chowdhury, B. Bose, K. Yamamoto, S.C. Veldhuis, Effect of interlayer thickness on nano-multilayer coating performance during high speed dry milling of H13 tool steel, Coatings 9 (2019) 737, https://doi.org/10.3390/coatings9110737.
[23] W. Heinke, A. Leyland, A. Matthews, G. Berg, C. Friedrich, E. Broszeit, Evaluation of PVD nitride coatings, using impact, scratch and Rockwell-C adhesion tests, Thin Solid Films 270 (1995) 431–438, https://doi.org/10.1016/0040-6090(95)06934-8.
[24] P. Drobný, D. Mercier, V. Koula, S.I. Škrobáková, L.' Caplovic, M. Sahul, Evaluation of adhesion properties of hard coatings by means of indentation and acoustic emission, Coatings 11 (2021) 919, https://doi.org/10.3390/coatings11080919.
[25] Y. Kravchenko, V. Borysiuk, A. Pogrebnjak, M. Kylyshkanov, I. Iatsunskyi, K. Smyrnova, Characteristics of arc-PVD TiAlSiY and (TiAlSiY)N coatings, in: IEEE 7th International Conference Nanomaterials: Application & Properties (NAP), 2017, https://doi.org/10.1109/NAP.2017.8190195, 01FNC02-1-01FNC02-4.
[26] Y. Sert, T. Küçükömeroğlu, İ. Efeoğlu, Investigating the structure, adhesion and tribological properties of Al and Zr-doped TiN coatings with various substrate bias voltage and working pressure, Proc. IME J. J. Eng. Tribol. (2020), https://doi.org/10.1177/1350650120940071.
[27] G. Cassar, S. Banfield, J.C. Avelar-Batista Wilson, J. Housden, A. Matthews, A. Leyland, Impact wear resistance of plasma diffusion treated and duplex treated/PVD-coated Ti–6Al–4V alloy, Surf. Coating. Technol. 206 (10) (2012) 2645–2654, https://doi.org/10.1016/j.surfcoat.2011.10.05.
[28] S. Barril, S. Mischler, D. Landolt, Triboelectrochemical investigation of the friction and wear behaviour of TiN coatings in a neutral solution, Tribol. Int. 34 (9) (2001) 599–608, https://doi.org/10.1016/s0301-679x(01)00052-.
[29] X. Shen, L. Cao, R. Li, Numerical simulation of sliding wear based on archard model, Int Conf. Mech. Automat. Control Engine. (2010) 325–329, https://doi.org/10.1109/MACE.2010.5535855.
[30] ASTM International, Standard Test Method for Linearly Reciprocating Ball-on-Flat Sliding Wear, G1vols. 33–05, 2016, pp. 1–9.
[31] B. J Hamrock, D. Dowson, Isothermal elastohydrodynamic lubrication of point contacts: Part III—fully flooded results, J. Lubrication Tech. 99 (1977) 264–275, https://doi.org/10.1115/1.3453074.
[32] A.A. Lubrecht, C.H. Venner, F. Colin, Film thickness calculation in elasto-hydrodynamic lubricated line and elliptical contacts: the Dowson, Higginson, Hamrock contribution, Proc. Inst. Mech. Eng. Part J J Eng Tribol 223 (2009) 511–515, https://doi.org/10.1243/13506501JET508.
[33] D. Dowson, M. Priest, G. Dalmaz, A.A. Lubrecht, Tribological Research and Design for Engineering Systems, Tribology Series, vol. 282, Elsevier, 2003, pp. 832–843, 41.
[34] S.G. Croll, Surface roughness profile and its effect on coating adhesion and corrosion protection: a review, Prog. Org. Coating 148 (2020), https://doi.org/10.1016/j.porgcoat.2020.105847.
[35] A. Jacob, S. Gangopadhyay, A. Satapathy, S. Mantry, B.B. Jha, Influences of micro-blasting as surface treatment technique on properties and performance of AlTiN coated tools, J. Manuf. Process. 29 (2017) 407–418, https://doi.org/10.1016/j.jmapro.2017.08.013.
[36] M. Raessi, J. Mostaghimi, M. Bussmann, Effect of surface roughness on splat shapes in the plasma spray coating process, Thin Solid Films 506–507 (2006) 133–135, https://doi.org/10.1016/j.tsf.2005.08.140.
[37] D. Yang, T. Chaolin, W. Yi, C. Ling, C. Panpan, K. Tongchun, L. Shumei, Z. Kesong, Effects of tailored nitriding layers on comprehensive properties of duplex plasma-treated AlTiN coatings, Ceram. Int. 43 (2017) 8721–8729, https://doi.org/10.1016/j.ceramint.2017.03.209.
[38] X. Guang, X. Ji, F. Hongyuan, J. Fan, G. Zhixing, Z. Haibo, X. Lijun, J. Zhengbiao, L. Jun, L. Yi, Investigations on microstructure, mechanical and tribological properties of TiN coatings deposited on three different tool materials, Int. J. Refract. Metals Hard Mater. 102 (2022), https://doi.org/10.1016/j.ijrmhm.2021.105700.
[39] E. Penilla, J. Wang, Pressure and temperature effects on stoichiometry and microstructure of nitrogen-rich TiN thin films synthesized via reactive magnetron DC-sputtering, J. Nanomater. (2008) 1–9, https://doi.org/10.1155/2008/267161.
[40] V. Teixeira, Residual stress and cracking in thin PVD coatings, Vacuum 64 (2002) 393–399, https://doi.org/10.1016/S0042-207X(01)00327-X.
[41] S.B. Kislitsin, A.I. Potekaev, V.V. Uglov, A.A. Klopotov, V.D. Klopotov, Y.F. Ivanov, A.T. Parpiev, Steel surface TiCrN, TiMoNcoatings structural phase state change features after low-energy alpha particles irradiation, IOP Conf. Ser. Mater. Sci. Eng. (2018) 289, https://doi.org/10.1088/1757-899x/289/1/012010.
[42] N. Witit-Anun, A. Teekhaboot, Effect of Ti sputtering current on structure of TiCrN thin films prepared by reactive DC magnetron Co-sputtering, in: Key Engineering Materials 675–676, 2016, pp. 181–184. https://doi.org/10.4028/www.scientific.net/kem.675-676.181.
[43] C. Paksunchai, S. Denchitcharoen, S. Chaiyakun, P. Limsuwan, Growth and characterization of nanostructured TiCrN films prepared by DC magnetron cosputtering, J. Nanomater. (2014) 1–9, https://doi.org/10.1155/2014/609482.
[44] J. Zheng, S.H. Zhang, P. Wu, S.C. Kwon, M.X. Li, S.Y. Liu, W.L. Chen, Microstructures and mechanical properties of duplex-treated composite ceramic coatings with and without compound layer, Ceram. Int. 41 (2) (2015) 2519–2526, https://doi.org/10.1016/j.ceramint.2014.10.07.
[45] L.N.M. Araújo, A.G.F. Araújo, M.O.G. Ferreira, R.R.M. Sousa, L.S. Cavalcante, L.C. C. Nunes, Effect of plasma nitriding time on the structural and mechanical properties of AISI-O1 steel, Eng. Rep. 2 (2020), https://doi.org/10.1002/eng2.12279.
[46] F.O. Ramírez-Reyna, G.A. Rodríguez-Castro, U. Figueroa-López, R.C. Morón, I. Arzate-Vázquez, A. Meneses-Amador, Effect of nitriding pretreatment on adhesion and tribological properties of AlCrN coating, Mater. Lett. (2020), 128931, https://doi.org/10.1016/j.matlet.2020.128931.
[47] A.P. de A. Manfridini, G.C.D. de Godoy, L. de A. Santos, Structural characterization of plasma nitrided interstitial-free steel at different temperatures by SEM, XRD and Rietveld method, J. Mater. Res. Technol. 6 (2017) 65–70, https://doi.org/10.1016/j.jmrt.2016.07.001.
[48] Y.Y. Chang, S. Amrutwar, Effect of plasma nitriding pretreatment on the mechanical properties of AlCrSiN-coated tool steels, Materials 12 (2019) 795, https://doi.org/10.3390/ma12050795.
[49] J.C. Caicedo, C. Amaya, L. Yate, M.E. Gómez, G. Zambrano, J. Alvarado-Rivera, P. Prieto, TiCN/TiNbCN multilayer coatings with enhanced mechanical properties, Appl. Surf. Sci. 256 (20) (2010) 5898–5904, https://doi.org/10.1016/j.apsusc.2010.03.071.
[50] Z. Chen, K. Zhou, X. Lu, Y.C. Lam, A review on the mechanical methods for evaluating coating adhesion, Acta Mech. 225 (2013) 431–452, https://doi.org/10.1007/s00707-013-0979-y.
[51] J. Matějíček, M. Vilémová, R. Mušálek, P. Sachr, J. Horník, The influence of interface characteristics on the adhesion/cohesion of plasma sprayed tungsten coatings, Coatings 3 (2) (2013) 108–125, https://doi.org/10.3390/coatings3020108.
[52] L. Bonin, V. Vitry, F. Delaunois, The Tin Stabilization Effect on the Microstructure, Corrosion and Wear Resistance of Electroless NiB Coatings, Surface and Coatings Technology, 2018, https://doi.org/10.1016/j.surfcoat.2018.10.011.
[53] A. Erdemir, J.M. Martin, Superior wear resistance of diamond and DLC coatings, Curr. Opin. Solid State Mater. Sci. (2018), https://doi.org/10.1016/j.cossms.2018.11.003.
[54] Y. Liu, S. Yu, Q. Shi, X. Ge, W. Wang, Multilayer coatings for tribology: a mini review, Nanomaterials 12 (2022) 1388, https://doi.org/10.3390/nano12091388.
[55] A. Thananan, A. Tatsuhiko, Y. Michiko, M. Atsushi, Y. Takahisa, I. Yuichi, Self-lubrication mechanism of chlorine implanted TiN coatings, Wear 254 (2003) 668–679, https://doi.org/10.1016/S0043-1648(03)00249-7.
[56] X. Wang, P.Y. Kwon, D. Schrock, D. Kim, Friction coefficient and sliding wear of AlTiN coating under various lubrication conditions, Wear 304 (2013) 67–76, https://doi.org/10.1016/j.wear.2013.03.050.
[57] Z. Chen, C. Gu, T. Tian, Modeling of formation and removal of ZDDP tribofilm on rough surfaces, Tribol. Lett. 69 (2021), https://doi.org/10.1007/s11249-020-01393-8.
[58] S.S. Saleem, M. Wani, M.J. Khan, Tribological investigations on tribofilm formation and retention under dry sliding conditions with increasing loads, Proc. Inst. Mech. Eng., Part L (2020), 146442072095183, https://doi.org/10.1177/1464420720951835.
[59] G. Ghosh, A. Sidpara, P.P. Bandyopadhyay, Understanding the role of surface roughness on the tribological performance and corrosion resistance of WC-Co coating, Surf. Coating. Technol. (2019), 125080, https://doi.org/10.1016/j.surfcoat.2019.125080.
[60] T. Khan, Y. Tamura, H. Yamamoto, A. Morina, A. Neville, Friction and wear mechanisms in boundary lubricated oxy-nitrided treated samples, Wear 368–369 (2016) 101–115, https://doi.org/10.1016/j.wear.2016.09.010.
[61] K. Ito, J.M. Martin, C. Minfray, K. Kato, Formation mechanism of a low friction ZDDP tribofilm on iron oxide, Tribol. Trans. 50 (2007) 211–216, https://doi.org/10.1080/10402000701271010.
[62] R. Gheisari, A.A. Polycarpou, Three-body abrasive wear of hard coatings: effects of hardness and roughness, Thin Solid Films 666 (2018) 66–75, https://doi.org/10.1016/j.tsf.2018.07.052.

Abbreviations

PVD: Physical Vapor Deposition
TiN: Titanium Nitride
TiCrN: Titanium Chromium Nitride
AFM: Atomic Force Microscope
SEM: Scanning Electron Microscope
EDX: Energy dispersive X-ray spectroscopy
XRD: X-ray diffraction
COF: Coefficient of friction
HRC: Hardness Rockwell C
ZDDP: Zincdithiophosphate
WR: Wear Rate

NOMENCLATURE

$E^{'}$: Effective elastic modulus, GPa
$E_{surface}$: Surface energy, nJ
h_{min}: Minimum oil film thickness, nm
L: Load, N
η_0: Dynamic viscosity, Pascal second, Pas
P_{max}: Maximum contact pressure, GPa
R: Radius, millimeter, mm
R_{qb}: Root mean square roughness of ball, nanometer, nm
R_{qs}: Root mean square roughness of sample, nanometer, nm
R_{tip}: Radius of the AFM tip
U: Sliding speed, meter per second, m/s
α: Pressure viscosity coefficient, m^2/N

S_a: Arithmetical mean height, nm
S_q: Root mean square height, nm
H: Hardness